Evolution of redox couples in Li- and Mn-rich cathode materials and mitigation of voltage fade by reducing oxygen release

Enyuan Hu [1,7], Xiqian Yu [1,2,7]*, Ruoqian Lin [1,3,7], Xuanxuan Bi [4], Jun Lu [4]*, Seongmin Bak [1], Kyung-Wan Nam [5], Huolin L. Xin [3]*, Cherno Jaye [6], Daniel A. Fischer [6], Kahlil Amine [4] and Xiao-Qing Yang [1]

Voltage fade is a major problem in battery applications for high-energy lithium- and manganese-rich (LMR) layered materials. As a result of the complexity of the LMR structure, the voltage fade mechanism is not well understood. Here we conduct both in situ and ex situ studies on a typical LMR material ($Li_{1.2}Ni_{0.15}Co_{0.1}Mn_{0.55}O_2$) during charge–discharge cycling, using multi-length-scale X-ray spectroscopic and three-dimensional electron microscopic imaging techniques. Through probing from the surface to the bulk, and from individual to whole ensembles of particles, we show that the average valence state of each type of transition metal cation is continuously reduced, which is attributed to oxygen release from the LMR material. Such reductions activate the lower-voltage Mn^{3+}/Mn^{4+} and Co^{2+}/Co^{3+} redox couples in addition to the original redox couples including Ni^{2+}/Ni^{3+}, Ni^{3+}/Ni^{4+} and O^{2-}/O^-, directly leading to the voltage fade. We also show that the oxygen release causes microstructural defects such as the formation of large pores within particles, which also contributes to the voltage fade. Surface coating and modification methods are suggested to be effective in suppressing the voltage fade through reducing the oxygen release.

L ithium- and manganese-rich (LMR) layer-structured cathode materials have been considered as one of the most promising candidates for high-energy-density lithium-ion batteries[1–4]. They can deliver reversible capacities of over $280\,mAh\,g^{-1}$, which almost double those of conventional cathode materials such as $LiCoO_2$ (ref. [5]) or $LiFePO_4$ (ref. [6]). However, these materials are still facing significant challenges for commercialization in large scale. One of the major problems is known as voltage fade, which means that on cycling, the discharge voltage of LMR materials keeps decreasing[7–9]. To overcome this problem, we need to acquire a fundamental understanding of the mechanism for voltage fade.

Numerous studies have been carried out to investigate this problem and the 'layered-to-spinel phase transition' has been considered as one of the main reasons for voltage fade. Xu et al.[10] observed the formation of a spinel phase on the surface of cycled LMR electrodes using aberration-corrected scanning transmission electron microscopy (STEM). Moreover, Gu et al.[11] observed spinel domains with different orientations within the same particle of cycled samples. On the basis of this observation, they proposed that the layered-to-spinel phase transition follows a nucleation and growth mechanism. In addition to these electron microscopy studies, Raman spectroscopic studies by Hong et al.[12] also provide evidence for such phase transition.

Since layered and spinel phases differ in how lithium and transition metal cations are arranged in each metal layer, layered-to-spinel phase transition indicates that the transition metal migration must be involved in this phase transition process[13]. Sathiya et al.[7] observed the trapping of transition metal ions in tetrahedral sites in cycled lithium-rich and ruthenium-rich samples (having very similar structure as LMR) using the STEM technique for comparative studies on two samples of $Li_2Ru_{0.75}Ti_{0.25}O_3$ and $Li_2Ru_{0.75}Sn_{0.25}O_3$. They found that there are more metal ions trapped in the $Li_2Ru_{0.75}Ti_{0.25}O_3$ sample than in the $Li_2Ru_{0.75}Sn_{0.25}O_3$ sample and attributed this result to the smaller ionic size of Ti^{4+} versus Sn^{4+}. Recently, Dogan et al.[8] identified the presence of tetrahedral occupation of the transition metal in the LMR material after the first charge using nuclear magnetic resonance spectroscopy and suggested that such local structural reorganization can lead to both voltage fade and hysteresis.

These studies provide valuable insight into the crystal structural changes relating to the voltage fade in LMR materials. However, the detailed relationship between such crystal structural changes and the voltage fade, the contribution to such fade by each element in the material during cycling, and how and where such structural reorganization starts and propagates through the particles of the cathode material during cycling have not been thoroughly studied yet.

Here, we carry out a systematic study on a typical LMR material $Li_{1.2}Ni_{0.15}Co_{0.1}Mn_{0.55}O_2$ by combining synchrotron X-ray absorption spectroscopy (XAS) with high penetration power and the capability to average through the whole cathode, STEM with atomic-level spatial resolution and the newly developed three-dimensional (3D) electron tomography[14]. A very large number of in situ and ex situ synchrotron X-ray spectra, from both hard XAS at transition metal K-edges and soft XAS at oxygen and carbon K-edges, were collected at various charge–discharge cycles and the capacity contribution from each transition metal redox couple was calculated for a certain

[1]Chemistry Division, Brookhaven National Laboratory, Upton, NY, USA. [2]Beijing National Laboratory for Condensed Matter Physics, Institute of Physics, Chinese Academy of Sciences, Beijing, China. [3]Center for Functional Nanomaterials, Brookhaven National Laboratory, Upton, NY, USA. [4]Chemical Sciences and Engineering Division, Argonne National Laboratory, Argonne, IL, USA. [5]Department of Energy and Materials Engineering, Dongguk University-Seoul, Seoul, Republic of Korea. [6]Material Measurement Laboratory, National Institute of Standards and Technology, Gaithersburg, MD, USA. [7]These authors contributed equally: Enyuan Hu, Xiqian Yu, Ruoqian Lin. *e-mail: xyu@iphy.ac.cn; junlu@anl.gov; hxin@bnl.gov

cycle number from these spectra. Comparing the charge–discharge profiles, we demonstrated that the origin of voltage fade is the redox couple evolution during cycling. We also investigated the evolution of microstructure during cycling and studied how that relates to the chemical degradation of the material. In addition, we demonstrated that the surface coating or other surface modifications are quite effective in suppressing the voltage fade through reducing the oxygen release during charge–discharge cycling.

Evolution of the redox couples during cycling

The electrochemistry of $Li_{1.2}Ni_{0.15}Co_{0.1}Mn_{0.55}O_2$ is plotted in Fig. 1, showing the typical voltage fade problem associated with LMR materials. The details are provided in Supplementary Note 1. The X-ray absorption near-edge structure spectra at the K-edges of Mn, Co and Ni were collected in situ during the 1st, 2nd, 25th, 46th and 83rd charge–discharge cycles. Detailed in situ data showing how the spectra of each transition metal element change during the charging and discharging process are shown in Supplementary Figs. 1–5. The results of these data at the end of charge and discharge for each of these cycles are plotted in Fig. 2 together with the ex situ data for the O K-edge for the same sample at the end of charge and discharge for each of these cycles. It can be seen clearly that with an increased number of cycles, the average valence states for all of these three transition metals are continuously reduced.

The oxygen fluorescence yield (FY) spectra show that most of the changes occur in the pre-edge region. There are continuous decreases in pre-edge peak intensity during cycling, indicating the weakening of the hybridization strength between the transition metal and the oxygen in the bulk. One thing to note is that in the post-edge region (peak centre at about 542 eV), the spectrum of the first cycle is different from other spectra of the subsequent cycles. This is probably due to the presence of oxygen vacancies in the materials, as has been discussed in previous reports[15,16]. A semi-quantitative analysis was carried out on the XAS data from the 1st, 2nd, 25th, 46th and 83rd cycles and the results are shown in Fig. 3a. The detailed analysis procedure is provided in Supplementary Note 2. In particular, the method of calculating the Mn oxidization state is shown in Supplementary Fig. 6.

In the initial cycle, oxygen and nickel are the two major contributors to the capacity, with $128\,mAh\,g^{-1}$ and $94\,mAh\,g^{-1}$ delivered capacity, respectively. However, on cycling, their roles become minor, with the capacity from oxygen decreasing to only $50\,mAh\,g^{-1}$ and the capacity from nickel decreasing to only $66\,mAh\,g^{-1}$ at the 83rd cycle. It is interesting to note that while the contributions from oxygen and nickel diminish, the contributions from manganese and cobalt steadily increase with their respective capacities going from $14\,mAh\,g^{-1}$ and $26\,mAh\,g^{-1}$ in the initial cycle to $66\,mAh\,g^{-1}$ and $53\,mAh\,g^{-1}$ in the 83rd cycle.

On the one hand, such a capacity increase from manganese and cobalt compensates the capacity loss from oxygen and nickel, maintaining the overall capacity during cycling. On the other hand, shifting the redox couples from oxygen and nickel to manganese and cobalt has a significant impact on the voltage profile, as illustrated in Fig. 3b, which shows how the density of states of the cathode material changes during cycling. The open-circuit voltage (OCV) in the Li battery is determined by the relative Fermi level energy with respect to the Li^+/Li^0 energy level, which is related to the work-function required to move the electrons from the cathode (LMR material) to the anode (lithium metal)[17]. For the pristine sample, the Fermi level lies just above the Ni^{2+}/Ni^{3+} redox couple. As the cycle goes on, oxygen loss occurs and leads to transition metal reduction. Specifically, nickel is likely to be reduced on the surface first, forming an electrochemically inactive rock-salt phase and decreasing the capacity contribution from nickel. Such a surface reconstruction process has been investigated in detail previously by Lin et al.[18]. For manganese and cobalt, their reduction resulted in the activation of the Mn^{3+}/Mn^{4+} and Co^{2+}/Co^{3+} redox couples. Such reductions shift
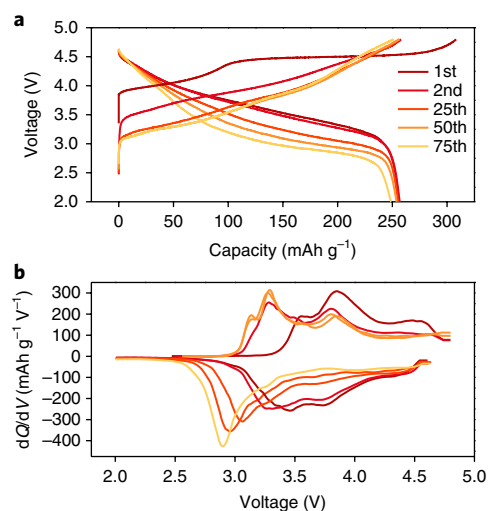
Fig. 1 | Electrochemical characterization of $Li_{1.2}Ni_{0.15}Co_{0.1}Mn_{0.55}O_2$.
a, Charge–discharge curves for $Li_{1.2}Ni_{0.15}Co_{0.1}Mn_{0.55}O_2$ for the 1st, 2nd, 25th, 50th and 75th cycles. **b**, dQ/dV plot of $Li_{1.2}Ni_{0.15}Co_{0.1}Mn_{0.55}O_2$ for the charge–discharge curves for the 1st, 2nd, 25th, 50th and 75th cycles.

the Fermi level higher and resulted in lower OCV and operating voltages. In fact, such process can also explain why the capacity contribution from oxygen is decreased: as transition metal is reduced, the covalency between the transition metal and oxygen is consequently weakened, causing less oxygen involvement in the redox reactions. One may notice that the difference between the energy levels is minimal for Ni^{2+}/Ni^{3+} and Ni^{3+}/Ni^{4+} redox couples but is very large for Co^{2+}/Co^{3+} and Co^{3+}/Co^{4+} and even larger for Mn^{3+}/Mn^{4+} and Mn^{4+}/Mn^{5+}. The reason for these larger differences can be explained by the schematic illustration of the electronic structures shown in Fig. 3c. It shows that for Mn and Co, different orbitals are involved when going from one redox couple to the other. For example, the Co^{2+}/Co^{3+} redox couple involves losing (oxidizing) or adding (reducing) an electron in the spin-up e_g orbital. However, the Co^{3+}/Co^{4+} redox couple involves losing (oxidizing) or adding (reducing) an electron in the spin-down t_{2g} orbital. However, for Ni, the same orbital (spin-up e_g) is involved in both Ni^{2+}/Ni^{3+} and Ni^{3+}/Ni^{4+} redox couples. Therefore, it is the reduction of Mn and Co that is mainly responsible for the drop in OCV or so-called voltage fade.

Surface reactions probed by soft XAS

While hard X-ray absorption provides rich information on the reaction in the bulk, the partial electron yield (PEY) mode of soft X-ray absorption can give complementary information about the surface. Spectra of O K-edge and C K-edge XAS collected in PEY mode are shown in Fig. 4a,b respectively. In O K-edge XAS, the pre-edge peaks (from 528 to 533 eV) arise from exciting an oxygen core shell $1s$ electron to unoccupied states that feature hybridization between oxygen $2p$ and transition metal $3d$ states. It is obvious that the pre-edge peak of the pristine sample is very similar to that of MnO_2, featuring a strong intensity. This was clearly explained by Luo et al.[4], who attributed such similarity to the high concentration of manganese at the surface and the great number of unoccupied $3d$ orbitals in tetravalent manganese. For the first cycle, when the sample was firstly charged, there is an increase in the pre-edge intensity, which arises both from the stronger hybridization between the oxygen $2p$ and the higher-valent transition metal and from the anionic redox reaction.

After the sample was discharged, the pre-edge intensity decreases reversibly (lower panel of Fig. 4a), suggesting that the top layer (around 5 nm, which is the probing depth of the PEY mode[19]) is still
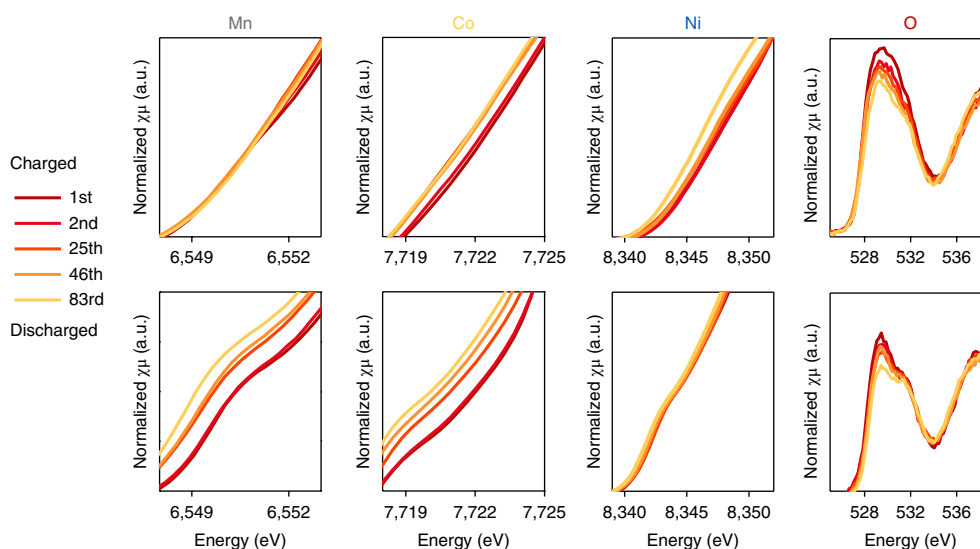
Fig. 2 | XAS results of various elements in $Li_{1.2}Ni_{0.15}Co_{0.1}Mn_{0.55}O_2$ at different cycles. K-edge XAS of Mn, Co, Ni and O for $Li_{1.2}Ni_{0.15}Co_{0.1}Mn_{0.55}O_2$ collected after the 1st, 2nd, 25th, 46th and 83rd cycles. For transition metals (Mn, Co and Ni), XAS is collected in the transmission mode; for oxygen, it is collected in the FY mode. For each element, charged and discharged graphs are plotted using the same scale.
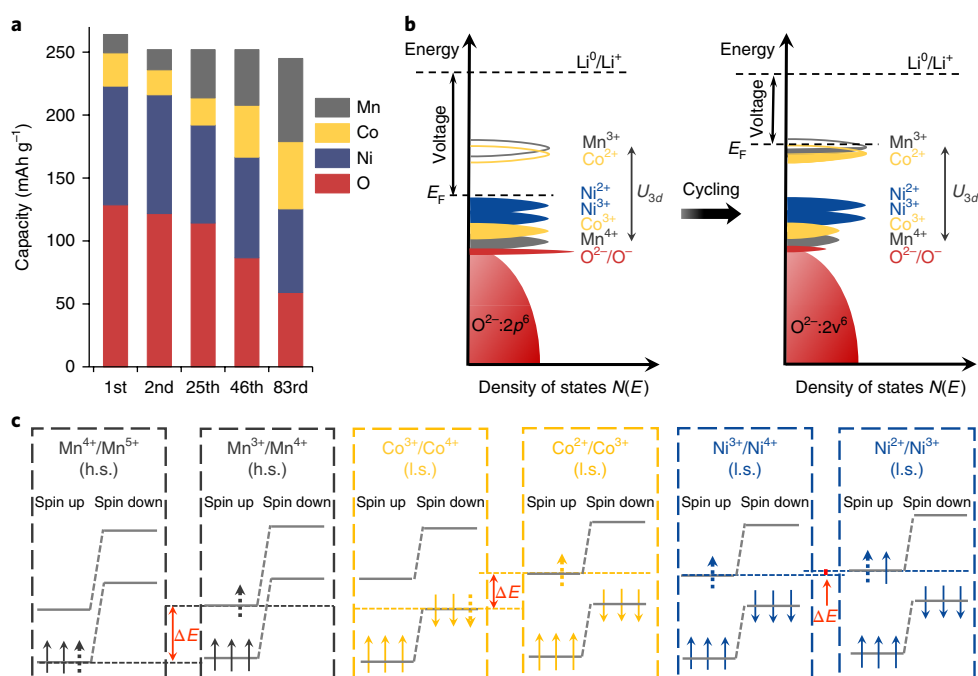
Fig. 3 | Redox couple evolution of $Li_{1.2}Ni_{0.15}Co_{0.1}Mn_{0.55}O_2$ during cycling. a, The contribution towards the discharge capacity from each element at various cycles. **b**, An illustration of the Fermi level being lifted up as a result of electronic structure change. As the voltage is determined by the energy gap between the Fermi level and the Li^+/Li^0 energy level, it is lowered accordingly. U_{3d} is the on-site Coulombic repulsion energy that splits up successive redox potentials. **c**, A diagram showing that, for different redox couples, Mn and Co would involve different energy levels. However, for Ni, the energy level is mostly the same. h.s. and l.s. are high spin and low spin, respectively.

mostly made up of active cathode materials during the 1st cycle. As the cycles goes on, the pre-edge peaks keep decreasing, which can be explained through two aspects. First, the surface reconstruction can take place during cycling, leading to the formation of rock-salt/spinel phases. This is supported by the PEY data for the transition metal L-edge shown in Supplementary Figs. 7–9. The transition metal valences are lower in these phases and consequently the hybridization strength between the transition metal $3d$ orbitals and the oxygen $2p$ orbitals is weakened. The second reason for the continuous decrease in the pre-edge intensity is the formation of various inorganic/organic compounds such as Li_2CO_3, Li_2O, LiOH, RCO_2Li and $R(OCO_2Li)_2$ (ref. [20]) as a result of electrolyte decomposition[21,22]. This argument is supported by the increase in the high-energy shoulder peaks (535 eV and above), a typical signature of surface OH species[23,24]. These oxygen-containing species do not have available orbitals to hybridize with oxygen $2p$ orbitals, leading to the absence of pre-edge peaks in their own O K-edge XAS spectra and an overall decrease in the pre-edge of the measured spectra.
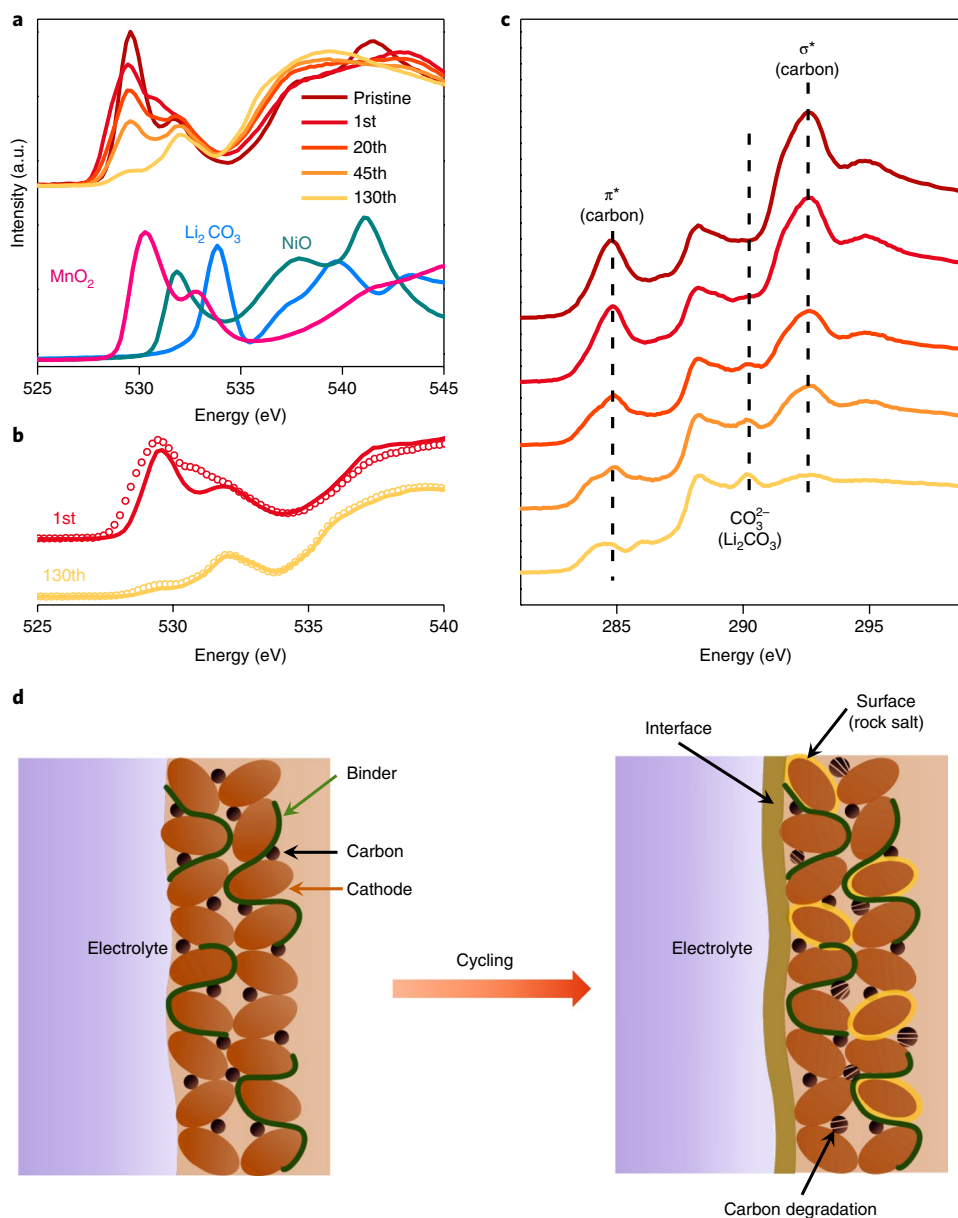
Fig. 4 | Surface degradation of Li₁.₂Ni₀.₁₅Co₀.₁Mn₀.₅₅O₂ leading to larger overpotential. a, PEY O K-edge XAS of samples from different cycles (charged state) with the reference spectra of MnO₂, and NiO and Li₂CO₃ shown. Note that during cycling, the pre-edge peaks (525—535 eV) keep decreasing and the shoulder peak around 537 eV keeps increasing. **b**, PEY O K-edge XAS spectra of charged (circle symbols) and discharged (lines) samples from the 1st and the 130th cycles. **c**, PEY C K-edge XAS spectra of samples from different cycles. **d**, An illustration of the interface formation and surface reconstruction of Li₁.₂Ni₀.₁₅Co₀.₁Mn₀.₅₅O₂ active material, as well as the degradation of carbon additive during cycling.

The surface reconstruction and the formation of the layer containing electrolyte decomposition compounds at the cathode/electrolyte interface (CEI) lead to a surface with gradually reduced electrochemical activity, as suggested by the greater and greater overlap between the spectrum of the charged sample and the discharged sample (Fig. 4b). The thickness of this inactive surface layer grows on cycling. By comparing the PEY data with the FY data (shown in Supplementary Figs. 10 and 11), it is estimated that the thickness can be up to tens of nanometres after 100 cycles.

The spectra of C K-edge XAS are shown in Fig. 4c. The peaks at 284.8 eV and at 292.6 eV are attributed to the π anti-bonding and the σ anti-bonding of the carbon additive[25,26]. The peak at 290.2 eV is attributed to the CO_3^{2-} in Li₂CO₃ (refs [27,28]). During cycling, there is a clear decrease in the peaks characteristic of the carbon additive. These observations suggest that the carbon additive keeps degrading

during cycling, presumably caused by intercalation of $(PF_6)^-$ into graphite at high voltage, which has been studied by Seel and Dahn[29]. In contrast, there is an increase in the peak belonging to Li₂CO₃, which is a major product in the CEI layer[28,30,31]. This peak intensity increase suggests that the CEI layer may grow during cycling, which is in agreement with previous O K-edge XAS results. The growth of the CEI layer can potentially make the whole electrochemical reaction more and more kinetically sluggish, causing an increase in the overpotential and a decrease in the observed discharge voltages.

The above results can be summarized in the illustration shown in Fig. 4d and are consistent with galvanostatic intermittent titration technique (GITT) measurements for cycled samples as shown in Supplementary Fig. 12, showing that surface degradation leads to an overpotential increase. Detailed discussions on GITT results are provided in Supplementary Note 3.
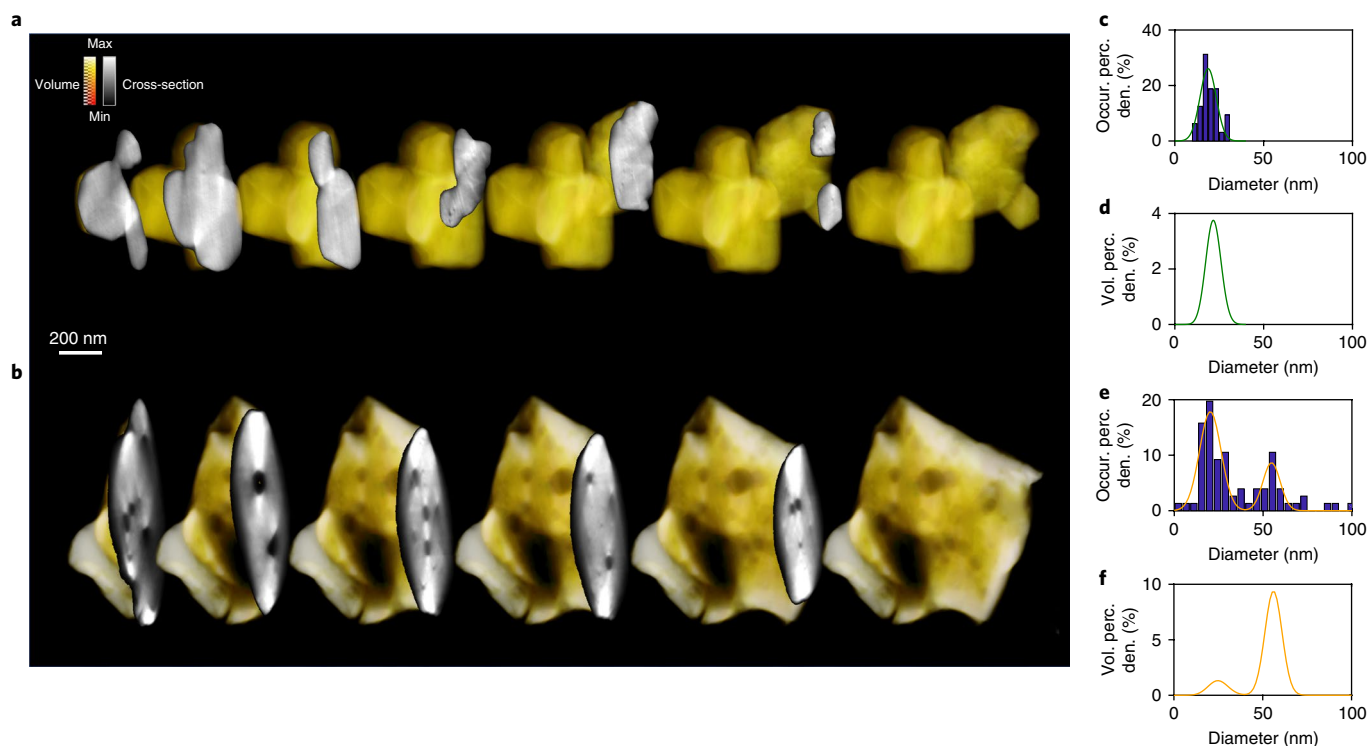
Fig. 5 | 3D electron tomography reconstruction of Li$_{1.2}$Ni$_{0.15}$Co$_{0.1}$Mn$_{0.55}$O$_2$ materials. a,b, A volume rendition and a progressive cross-sectional view of cathode particles in the pristine state (**a**) and after 15 cycles (**b**). **c,d**, The internal pore size distribution of the pristine sample weighted by occurrence (**c**) and by volume (**d**). **e,f**, The internal pore size distribution of the cycled sample (15 cycles) weighted by occurrence (**e**) and by volume (**f**). The green and orange lines in **c** and **e** are single-Gaussian and bi-Gaussian fitting of the pore size histogram. The reweighting by volume in **d** and **f** is applied to the fitted curves.

Initiation and propagation of microstructural degradation

All of the spectroscopic evidence stated above and the results reported in the literature point out that the voltage fade is caused by the oxygen loss and consequential transition metal reduction during cycling. However, where and how the oxygen-loss-induced microstructure changes take place in cathode material and propagate have not been thoroughly studied. To pinpoint the structure nucleation and evolution, we performed atomic-resolution annular dark-field STEM (ADF-STEM) imaging, spatially resolved electron energy-loss spectroscopy (EELS) and ADF-STEM tomography.

Using ADF-STEM tomography, the 3D internal structures of the cathode material before and after 15 charge–discharge cycles were reconstructed (Fig. 5a,b). The 3D rendered reconstructions shown in Fig. 5b qualitatively show that a new population of large pores had formed in the interior of the cycled particle after 15 cycles. By analysing the pore size distributions (Fig. 5c–f), it can be quantitatively concluded that the large pores observed in Fig. 5b belong to a new mode that did not appear in the pristine samples. The volume-weighted distribution shows that the large pores contribute to the majority of porosity in the material. As the formation of the large pores is correlated with charge cycles, they are very likely formed by nucleating vacancies that had been left behind by oxygen loss, agreeing well with the 'lattice densification' model proposed by Delmas and co-workers[32]. To estimate how much oxygen is lost from the lattice to create these pores, we selected several particles and calculated their pore fractions. It is found that the pore fraction varies from 1.5% to 5.2%, indicating that the maximum amount of oxygen loss can be as large as 9% after cycling (the detailed methodology to evaluate the amount of oxygen loss is provided in Supplementary Note 4). It is worth noting that the pore distribution evolution is found in multiple particles (Supplementary Fig. 13).

Therefore, the results presented here are statistically reliable. In addition to the estimation, we performed differential electrochemical mass spectrometry (DEMS) to directly observe whether the oxygen loss is in the form of gas release from the material lattice, shown in Supplementary Fig. 14a. A trace amount of oxygen was detected after full charge of each cycle (Supplementary Fig. 14b), indicating continuous oxygen loss during cycling. The detailed DEMS measurement is explained in Supplementary Note 5.

To further clarify the origin of these pores, STEM-EELS mapping of a concealed pore and an exposed pore was performed as shown in Fig. 6. Figure 6a shows the STEM-EELS mapping results over a concealed pore in the bulk and the exposed pore at the surface of the particle. The EELS map of the concealed pore shows that there is only a very thin shell of Mn^{2+} build-up around the pore (Fig. 6a). Since a significant number of small pores were observed in the pristine sample before cycling, it is assumed that these internal concealed pores are formed during synthesis and may keep their size and shape unchanged during cycling until oxygen release is initiated near them. In contrast, for the opposite extreme situation in an exposed pore, the entire pore surface area is exposed to the electrolyte, as shown in Fig. 6b, and a thick layer of spinel/rock-salt structure phase was formed through the interaction between the pore surface and the electrolyte. The EELS relative concentration mapping shows that there is a significant increase in Mn relative concentration close to the surface volume. Based on the fact that the number of large pores increases during cycling as shown in Fig. 5, we can speculate that a large number of pores are neither completely concealed nor completely exposed. Instead, they are partially exposed pores with oxygen diffusion pathways nearby in the form of microstructural defects such as dislocation, grain boundaries and micro cracks. During cycling, these partially exposed pores will
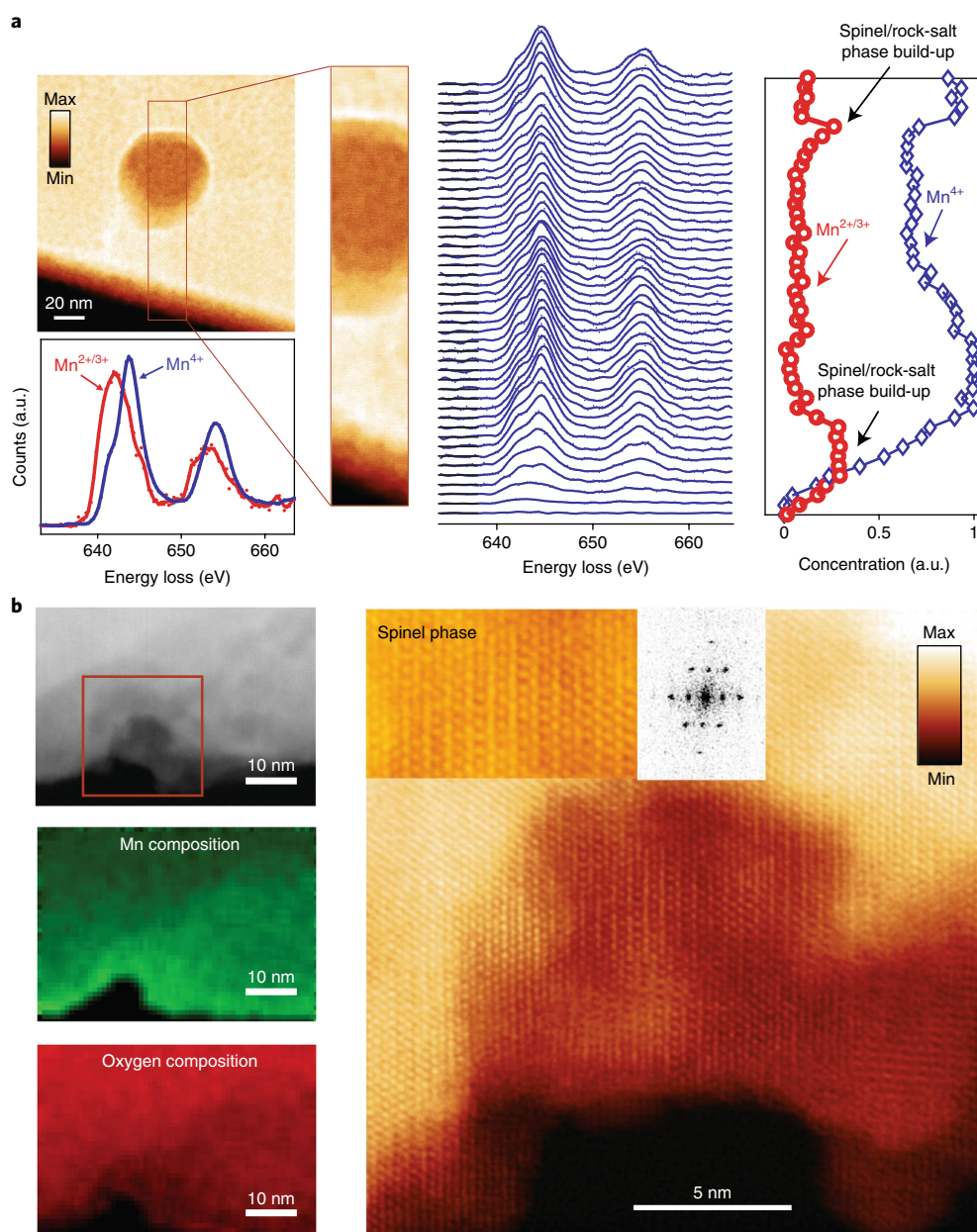
Fig. 6 | Spatially resolved EELS mapping of concealed and exposed pores. a, STEM-EELS mapping of a concealed pore. Top left: an ADF-STEM image of a concealed pore. Bottom left: the reference spectra used for linear composition of the Mn $L_{2,3}$ spectra in the middle panel. Middle: the EELS spectra of Mn $L_{2,3}$-edges across the surface and the concealed pore. Right: the linear decomposition coefficient as a function of the vertical spatial location. **b**, STEM-EELS mapping and atomic-resolution imaging of an exposed pore. Top left: an ADF-STEM image of an opened pore. Middle and bottom left: the Mn (middle) and oxygen (bottom) composition extracted from the quantification of the EELS map. Right: atomic-resolution image of the open pore.

grow in size and number, together with those completely exposed pores at the surface, contributing to the propagation of the structural phase transitions, facilitating the further oxygen loss and self-feeding the further microstructural defect formation, as well as accelerating the voltage fade.

Discussion

The role of manganese in voltage fade has been well studied and it is understood that manganese goes through reduction on oxygen loss and the Mn^{2+} cations resulting from the disproportionation reaction ($Mn^{3+} \rightarrow Mn^{2+} + Mn^{4+}$) migrate more easily to the tetrahedral site[8,33,34]. However, not enough attention has been paid to the role of cobalt on such voltage fade. As a matter of fact, cobalt has been

known to be beneficial in stabilizing the layer structure, and it is widely used in layer-structured cathode materials[35,36]. Therefore, the role of Co in voltage fade is quite important.

Here, it is clearly shown that during cycling, cobalt also experiences reduction and directly contributes to the voltage fade by shifting the redox couple from Co^{3+}/Co^{4+} to Co^{2+}/Co^{3+}.

The continued transition metal reduction during cycling indicates on-going oxygen loss at the same time. This is unambiguously confirmed by the 3D TEM electron tomography and spatially resolved EELS mapping. Most of the TEM studies reported in the literature are 2D, limited to provide the statistics of the pore size distribution. Powered by the newly developed 3D electron tomography, we are able to visualize the growing size of the pores during
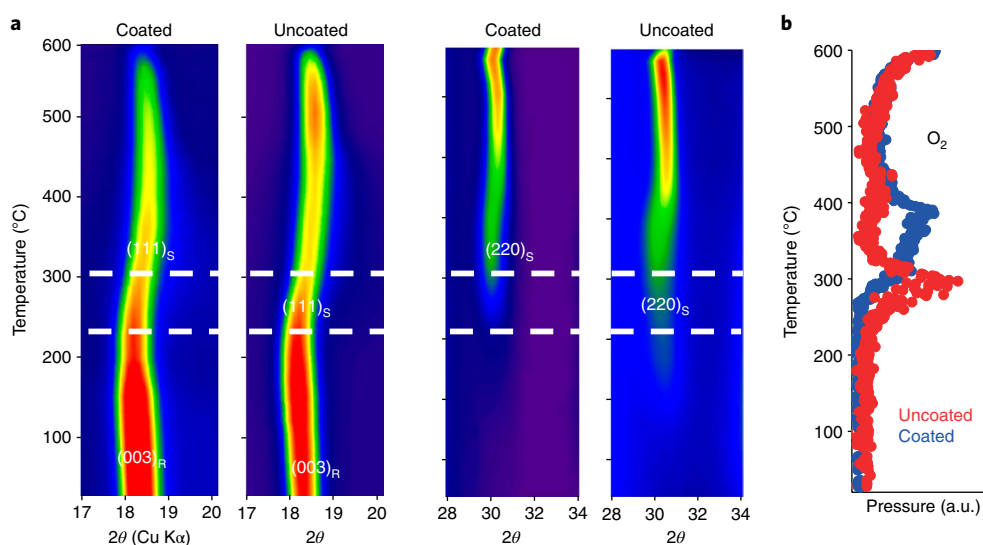
Fig. 7 | Thermal stability comparison between uncoated and AlF₃-coated Li₁.₂Ni₀.₁₅Co₀.₁Mn₀.₅₅O₂. a, XRD results of the two materials (both are in charged states) during the in situ heating experiment, showing that the uncoated sample goes through the phase transition earlier than the coated one. R stands for rhombohedral phase (R$\bar{3}$m) and S stands for spinel phase (Fd$\bar{3}$m). **b**, Oxygen gas evolution of the two samples during the in situ heating experiment, showing that the uncoated sample releases oxygen at a lower temperature than the coated one.

cycling and the nucleation and propagation of the new spinel phase at the interface between the surface of the exposed pore and the electrolyte. It has been proposed that microstructural defects, oxygen release and spinel phase formation are closely related factors and they can facilitate each other during cycling[9]. Results from this work are in very good agreement with those reported in our previously published papers using 3D transmission X-ray microscopic tomography[37,38]. A schematic illustration of the comprehensive spectroscopic techniques used and the results obtained from these studies are shown in Supplementary Fig. 15. The morphological change induced by oxygen release can influence the voltage fade in two ways. First, it exposes more surfaces and creates more defects in the particle, both of which promote further oxygen loss. Oxygen loss, in turn, leads to transition metal reduction that contributes to voltage fade. Second, a porosity increase can give rise to more cracks within the particle, weakening the contact between the active material and the carbon additive/current collector[39–41]. This would lead to an electric resistance increase in the cell and contribute to the deteriorated electrochemical performance through the increased overpotential.

From the above discussion, it is clear that oxygen loss plays a critical role in voltage fade. It contributes to voltage fade by reducing manganese and cobalt followed by activating the Mn³⁺/Mn⁴⁺ and Co²⁺/Co³⁺ redox couples at lower voltages. In addition, it slows down the charge transfer across the CEI and deteriorates the electrochemical performance by reducing nickel and facilitates the surface reconstruction. Therefore, suppressing oxygen loss would be a very effective approach to reduce voltage fade in LMR materials.

Practically, there are two good approaches to tackle oxygen loss. First, surface modification is a relatively simple process to reduce oxygen release at the surface of particles. For example, there are several reports showing how surface coating can suppress voltage fade in LMR materials. Considering that oxygen loss can be facilitated by defects causing larger electrolyte-interacting areas, it would be even more desirable to have the coating at the primary particle level, not just at the secondary particle level. It is interesting to note that there is recent progress in this direction as reported by Kajiyama et al.[42]. Aside from coating, there are other surface treatment methods. For example, Qiu et al.[43] recently demonstrated that a surface treatment

that introduces more oxygen vacancy on the particle's surface can significantly decrease the scale of oxygen loss and effectively suppress voltage fade.

Second, as oxygen loss is usually associated with phase transition of the bulk material, it is possible to indirectly suppress oxygen loss by kinetically manipulating the phase transition. This can be achieved by introducing appropriate foreign elements into the bulk material. This argument is supported by a recent example reported by Nayak et al.[44]. These authors demonstrate the effectiveness of aluminium doping in suppressing voltage fade. Another example is a paper published by Hu et al.[45] that pointed out that oxygen loss during heating can be suppressed by doping the material with cations that have tendencies to occupy tetrahedral sites. The tetrahedral site occupation of these cations could hinder the transition metal cation migration through tetrahedral sites, which is considered as a parallel process for the phase transition to the spinel structure accompanied with oxygen loss.

Although these design principles provide important directions for material design, the practical optimization of the LMR material synthesis still involves many trial-and-error efforts. It would be highly desirable to predict the long cycling behaviour of LMR materials by some simple methods without going through the long-time cycling. It is interesting to note that similar oxygen release and transition metal reduction processes are also observed in experiments when heating up the charged cathode materials[46,47]. In those thermal stability studies, it was found that transition metals, particularly manganese and cobalt, migrate to tetrahedral sites, leading to the formation of spinel phases. Such migration has also been observed in the cycling experiments, but at a smaller scale and usually takes more effort to characterize[7]. The similar responses of the cathode material to external forces (voltage in the case of cycling or temperature in the case of heating) have been explored by Schilling and Dahn[48], Ceder and co-workers[49] and Yang and co-workers[50]. On the basis of these studies, it might be possible to speed up the material screening test by associating the electrochemical cycling performance with the thermal stability. Instead of characterizing the stability of the cathode material by going through many electrochemical cycles, a heating experiment (within hours) can be performed on the material to reveal its thermal stability. This can serve

as a strong indicator of the electrochemical performance. There are several examples in the literature showing that doping and surface coating can effectively mitigate the voltage fade problem in LMR materials[44,51–53]. For example, previous work by Zheng et al.[53] indicates that AlF_3 coating can effectively suppress the voltage fade in LMR material as shown in Supplementary Fig. 16.

To summarize, we demonstrated in this work that such performance improvement in reducing the voltage fade during electrochemical cycling can be well correlated with the improvement in thermal stability. As shown in Fig. 7 (detailed in situ XRD data covering the full 2θ range is shown in Supplementary Fig. 16), the uncoated LMR material experiences layered-to-spinel phase transition (illustrated by the appearance of the (220) peak that is characteristic of spinel) and oxygen release at a much lower temperature than the temperature observed for oxygen release in the AlF_3-coated system, indicating that coated LMR is more thermally stable. Such a correlation between electrochemical cycling and thermal stability is not a coincidence but intrinsically caused by the fact that both cycling and heating can involve oxygen loss, and transition metal reduction and migration. This correlation provides a simple and quick procedure to test the effectiveness of a new surface modification or a new material developed to suppress voltage fade without having to conduct time-consuming multiple cycling: if the material for surface modification has a better thermal stability (meaning that oxygen is released only at high temperature), it would have a better structural stability in resisting voltage fade during cycling.

Methods

Electrochemical measurement. The $Li_{1.2}Ni_{0.15}Co_{0.1}Mn_{0.55}O_2$ cathode electrodes were prepared by slurrying the active material, carbon black and polyvinylidene fluoride with a weight ratio of 86:6:8 in N-methyl pyrrolidone solvent, and then coating the mixture onto an Al foil. High-purity lithium foil was used as the anode. The electrolyte was 1.2 mol $LiPF_6$ in ethylene carbonate and dimethyl carbonate solvent (3:7 by volume, Novolyte Inc.). The 2032-type button cells for electrochemical studies were assembled in an argon-filled glove box and tested on a VMP3 BioLogic electrochemistry workstation. GITT experiments (Biologic Inc.) were performed by charging/discharging the cell for 1 h at a current density of 21 mAg^{-1} and relaxing it for 12 h to reach a quasi-equilibrium state and then repeating this process until the voltage limitation was reached.

X-ray absorption spectroscopy. The hard XAS experiments were carried out at beamline X18A of the National Synchrotron Light Source (NSLS) at Brookhaven National Laboratory. The in situ XAS experiments were performed in transmission mode using a Si (111) double-crystal monochromator detuned to 35–45% of its original maximum intensity to eliminate the high-order harmonics. A reference spectrum for each element was simultaneously collected with the corresponding spectrum of the in situ cells using transition metal foil. The energy calibration was carried out using the first inflection point of the K-edge spectrum of the transition metal foil as a reference. The XANES and extended X-ray absorption fine-structure data were analysed using the ATHENA[54] software package. The soft XAS measurements were performed in both FY and PEY modes at beamline U7A of the NSLS. The beam size was 1 mm in diameter. The estimated incident X-ray energy resolution was ~0.15 eV at the O K-edge. The monochromator absorption features and beam instabilities were normalized for both FY and PEY signals by dividing the detected FY and PEY signals by the photoemission current of a clean gold Io mesh placed in the incident beam. The energy calibration was carried out by initially calibrating the principal monochromator Io oxygen absorption feature to 531.2 eV using an oxygen gas-phase absorption cell. An additional Io mesh of Ni was also placed in the incident beam to ensure energy calibration (based on the oxygen calibration above) and energy-scale reproducibility of the many PEY or FY spectra presented. The PEY data were recorded using a channel electron multiplier equipped with a three-grid high-pass electron kinetic energy filter, while the FY data were recorded using a windowless energy dispersive Si (Li) detector. A linear background fit to the pre-edge region was subtracted from the spectra. The O K-edge spectra are normalized between 585 and 630 eV.

In situ time-resolved XRD and mass spectroscopy. The charged cells were transferred to a glove box for disassembly. The charged cathodes were washed in dimethyl carbonate solvent in the glove box and the fine cathode powders (including the binder and conductive carbon) were obtained by scratching away the electrode from the current collector. They were loaded into 0.5-mm-diameter quartz capillaries in the glove box and the capillary tip was sealed temporarily

with vacuum grease in the glove box. The capillary then was transferred from the glove box and hermetically sealed using an oxygen torch before being mounted on the thermal stage of beamline X7B, at the National Synchrotron Light Source (NSLS), Brookhaven National Laboratory. The detailed experimental procedure is described in a previous report[39].

TEM characterization. Atomic-resolution annular dark-field STEM imaging, and spatially resolved electron energy-loss spectroscopic mapping were performed on a 200-keV probe-corrected dedicated STEM equipped with a cold field emitter and an Enfina spectrometer. The electron tomography results were acquired in a 200 keV S/TEM with a Schottky field emitter. For each 3D reconstruction, a tilt series of 71 images were acquired in the annular dark-field STEM mode from −70 degrees to +70 degrees with 2-degree intervals. The tomograms were reconstructed using a custom-written MATLAB script that implements a multiplicative simultaneous iterative reconstruction technique.

Data availability. The data that support the plots within this paper and other finding of this study are available from the corresponding author upon reasonable request.

References

1. Lu, Z. & Dahn, J. R. Understanding the anomalous capacity of Li/Li[NixLi$_{(1/3-2x/3)}$ Mn$_{(2/3-x/3)}$]O$_2$ cells using in situ X-ray diffraction and electrochemical studies. *J. Electrochem. Soc.* **149**, A815–A822 (2002).
2. Thackeray, M. M. et al. Li$_2$MnO$_3$-stabilized LiMO$_2$ (M= Mn, Ni, Co) electrodes for lithium-ion batteries. *J. Mater. Chem.* **17**, 3112–3125 (2007).
3. Sathiya, M. et al. Reversible anionic redox chemistry in high-capacity layered-oxide electrodes. *Nat. Mater.* **12**, 827–835 (2013).
4. Luo, K. et al. Charge-compensation in 3*d*-transition-metal-oxide intercalation cathodes through the generation of localized electron holes on oxygen. *Nat. Chem.* **8**, 684–691 (2016).
5. Mizushima, K., Jones, P., Wiseman, P. & Goodenough, J. B. Li$_x$CoO$_2$ (0<x≤1): A new cathode material for batteries of high energy density. *Mater. Res. Bull.* **15**, 783–789 (1980).
6. Padhi, A. K., Nanjundaswamy, K. & Goodenough, J. Phospho-olivines as positive electrode materials for rechargeable lithium batteries. *J. Electrochem. Soc.* **144**, 1188–1194 (1997).
7. Sathiya, M. et al. Origin of voltage decay in high-capacity layered oxide electrodes. *Nat. Mater.* **14**, 230–238 (2015).
8. Dogan, F. et al. Re-entrant lithium local environments and defect driven electrochemistry of Li-and Mn-Rich Li-ion battery cathodes. *J. Am. Chem. Soc.* **137**, 2328–2335 (2015).
9. Hu, E. Y. et al. Explore the effects of microstructural defects on voltage fade of Li- and Mn-rich cathodes. *Nano Lett.* **16**, 5999–6007 (2016).
10. Xu, B., Fell, C. R., Chi, M. F. & Meng, Y. S. Identifying surface structural changes in layered Li-excess nickel manganese oxides in high voltage lithium ion batteries: A joint experimental and theoretical study. *Energy Environ. Sci.* **4**, 2223–2233 (2011).
11. Gu, M. et al. Formation of the spinel phase in the layered composite cathode used in Li-ion batteries. *ACS Nano* **7**, 760–767 (2013).
12. Hong, J. et al. Structural evolution of layered Li$_{1.2}$Ni$_{0.2}$Mn$_{0.6}$O$_2$ upon electrochemical cycling in a Li rechargeable battery. *J. Mater. Chem.* **20**, 10179–10186 (2010).
13. Reed, J. & Ceder, G. Role of electronic structure in the susceptibility of metastable transition-metal oxide structures to transformation. *Chem. Rev.* **104**, 4513–4533 (2004).
14. Li, H. Y., Xin, H. L., Muller, D. A. & Estroff, L. A. Visualizing the 3D internal structure of calcite single crystals grown in agarose hydrogels. *Science* **326**, 1244–1247 (2009).
15. Ruckman, M. W. et al. Interpreting the near edges of O$_2$ and O$_2^-$ in alkali-metal superoxides. *Phys. Rev. Lett.* **67**, 2533–2536 (1991).
16. Palina, N. et al. Electronic defect states at the LaAlO$_3$/SrTiO$_3$ heterointerface revealed by O K-edge X-ray absorption spectroscopy. *Phys. Chem. Chem. Phys.* **18**, 13844–13851 (2016).
17. Goodenough, J. B. Evolution of strategies for modern rechargeable batteries. *Acc. Chem. Res.* **46**, 1053–1061 (2013).
18. Lin, F. et al. Surface reconstruction and chemical evolution of stoichiometric layered cathode materials for lithium-ion batteries. *Nat. Commun.* **5**, 3529 (2014).
19. Yoon, W. S. et al. In situ soft XAS study on nickel-based layered cathode material at elevated temperatures: A novel approach to study thermal stability. *Sci. Rep.* **4**, 6827 (2014).
20. Aurbach, D., Daroux, M., Faguy, P. & Yeager, E. The electrochemistry of noble metal electrodes in aprotic organic solvents containing lithium-salts. *J. Electroanal. Chem.* **297**, 225–244 (1991).

21. Browning, J. F. et al. In situ determination of the liquid/solid interface thickness and composition for the Li ion cathode LiMn$_{1.5}$Ni$_{0.5}$O$_4$. *ACS Appl. Mater. Interface.* **6**, 18569–18576 (2014).

22. Yamamoto, K. et al. Improved cyclic performance of lithium-ion batteries: an investigation of cathode/electrolyte interface via in situ total-reflection fluorescence X-ray absorption spectroscopy. *J. Phys. Chem. C* **118**, 9538–9543 (2014).

23. Qiao, R. M. et al. Distinct solid-electrolyte-interphases on Sn (100) and (001) electrodes studied by soft X-ray spectroscopy. *Adv. Mater. Interfaces* **1**, 1300115 (2014).

24. Li, Q. H. et al. Quantitative probe of the transition metal redox in battery electrodes through soft x-ray absorption spectroscopy. *J. Phys. D* **49**, 413003 (2016).

25. Nithianandam, J., Rife, J. C. & Windischmann, H. Carbon-K edge spectroscopy of internal interface and defect states of chemical vapor-deposited diamond films. *Appl. Phys. Lett.* **60**, 135–137 (1992).

26. Chiou, J. W. et al. Electronic structure of the carbon nanotube tips studied by X-ray-absorption spectroscopy and scanning photoelectron microscopy. *Appl. Phys. Lett.* **81**, 4189–4191 (2002).

27. Gallant, B. M. et al. Chemical and morphological changes of Li-O$_2$ battery electrodes upon cycling. *J. Phys. Chem. C* **116**, 20800–20805 (2012).

28. Gauthier, M. et al. Electrode–electrolyte interface in Li-ion batteries: current understanding and new insights. *J. Phys. Chem. Lett.* **6**, 4653–4672 (2015).

29. Seel, J. A. & Dahn, J. R. Electrochemical intercalation of PF$_6$ into graphite. *J. Electrochem. Soc.* **147**, 892–898 (2000).

30. Busche, M. R. et al. Dynamic formation of a solid–liquid electrolyte interphase and its consequences for hybrid-battery concepts. *Nat. Chem.* **8**, 426–434 (2016).

31. Aurbach, D. Review of selected electrode-solution interactions which determine the performance of Li and Li ion batteries. *J. Power Sources* **89**, 206–218 (2000).

32. Tran, N. et al. Mechanisms associated with the "plateau" observed at high voltage for the overlithiated Li$_{1.12}$(Ni$_{0.425}$Mn$_{0.425}$Co$_{0.15}$)$_{0.88}$O$_2$ system. *Chem. Mater.* **20**, 4815–4825 (2008).

33. Yu, X. Q. et al. Understanding the rate capability of high-energy-density Li-rich layered Li$_{1.2}$Ni$_{0.15}$Co$_{0.1}$Mn$_{0.55}$O$_2$ cathode materials. *Adv. Energy Mater.* **4**, 1300950 (2014).

34. Rozier, P. & Tarascon, J. M. Review—Li-rich layered oxide cathodes for next-generation Li-ion batteries: chances and challenges. *J. Electrochem. Soc.* **162**, A2490–A2499 (2015).

35. Lee, E. S. & Manthiram, A. Smart design of lithium-rich layered oxide cathode compositions with suppressed voltage decay. *J. Mater. Chem. A* **2**, 3932–3939 (2014).

36. Saadoune, I. & Delmas, C. LiNi$_{1-y}$Co$_y$O$_2$ positive electrode materials: relationships between the structure, physical properties and electrochemical behaviour. *J. Mater. Chem.* **6**, 193–199 (1996).

37. Xu, Y. et al. Structural integrity—searching the key factor to suppress the voltage fade of Li-rich layered cathode materials through 3D X-ray imaging and spectroscopy techniques. *Nano Energy* **28**, 164–171 (2016).

38. Xu, Y. et al. In situ visualization of state-of-charge heterogeneity within a LiCoO$_2$ particle that evolves upon cycling at different rates. *ACS Energy Lett.* **2**, 1240–1245 (2017).

39. Yan, P. F. et al. Intragranular cracking as a critical barrier for high-voltage usage of layer-structured cathode for lithium-ion batteries. *Nat. Commun.* **8**, 14101 (2017).

40. Zheng, J. M. et al. Corrosion/fragmentation of layered composite cathode and related capacity/voltage fading during cycling process. *Nano Lett.* **13**, 3824–3830 (2013).

41. Chen, C. J. et al. The origin of capacity fade in the Li$_2$MnO$_3$·LiMO$_2$ (M=Li, Ni, Co, Mn) microsphere positive electrode: an operando neutron diffraction and transmission X-ray microscopy study. *J. Am. Chem. Soc.* **138**, 8824–8833 (2016).

42. Kim, H., Kim, M. G., Jeong, H. Y., Nam, H., & Cho, J. A new coating method for alleviating surface degradation of LiNi$_{0.6}$Co$_{0.2}$Mn$_{0.2}$O$_2$ cathode material: nanoscale surface treatment of primary particles. *Nano Lett.* **15**, 2111–2119 (2015).

43. Qiu, B. et al. Gas–solid interfacial modification of oxygen activity in layered oxide cathodes for lithium-ion batteries. *Nat. Commun.* **7**, 12108 (2016).

44. Nayak, P. K. et al. Al doping for mitigating the capacity fading and voltage decay of layered Li and Mn-rich cathodes for Li-ion batteries. *Adv. Energy Mater.* **6**, 1502398 (2016).

45. Hu, E. Y. et al. Utilizing environmental friendly iron as a substitution element in spinel structured cathode materials for safer high energy lithium-ion batteries. *Adv. Energy Mater.* **6**, 1501662 (2016).

46. Nam, K. W. et al. Combining in situ synchrotron X-ray diffraction and absorption techniques with transmission electron microscopy to study the origin of thermal instability in overcharged cathode materials for lithium-ion batteries. *Adv. Funct. Mater.* **23**, 1047–1063 (2013).

47. Hu, E. Y. et al. Oxygen-release-related thermal stability and decomposition pathways of Li$_x$Ni$_{0.5}$Mn$_{1.5}$O$_4$ cathode materials. *Chem. Mater.* **26**, 1108–1118 (2014).

48. Schilling, O. & Dahn, J. R. Thermodynamic stability of chemically delithiated Li(Li$_x$Mn$_{2-x}$)O$_4$. *J. Electrochem. Soc.* **145**, 569–575 (1998).

49. Wang, L., Maxisch, T. & Ceder, G. A first-principles approach to studying the thermal stability of oxide cathode materials. *Chem. Mater.* **19**, 543–552 (2007).

50. Bak, S. M. et al. Structural changes and thermal stability of charged LiNi$_x$Mn$_y$Co$_z$O$_2$ cathode materials studied by combined in situ time-resolved XRD and mass spectroscopy. *ACS appl. Mater. Interfaces.* **2014**, 22594–22601 (2014).

51. Kim, J. H. et al. Effect of aluminum fluoride coating on the electrochemical and thermal properties of 0.5Li$_2$MnO$_3$·0.5LiNi$_{0.5}$Co$_{0.2}$Mn$_{0.3}$O$_2$ composite material. *J. Alloys Compd.* **517**, 20–25 (2012).

52. Kim, H. B. et al. Electrochemical and thermal characterization of AlF$_3$-coated Li[Ni$_{0.8}$Co$_{0.15}$Al$_{0.05}$]O$_2$ cathode in lithium-ion cells. *J. Power Sources* **179**, 347–350 (2008).

53. Zheng, J. M. et al. Functioning mechanism of AlF$_3$ coating on the Li- and Mn-rich cathode materials. *Chem. Mater.* **26**, 6320–6327 (2014).

54. Ravel, B. & Newville, M. ATHENA, ARTEMIS, HEPHAESTUS: data analysis for X-ray absorption spectroscopy using IFEFFIT. *J. Synchrotron Radiat.* **12**, 537–541 (2005).

Author contributions

X.Y. and X.-Q.Y. designed the work; X.Y. and J.L. performed the electrochemical measurements; X.Y. and K.-W.N. performed the hard X-ray in situ XAS experiments; X.Y., S.B., K.-W.N., C.J. and D.A.F. performed the soft XAS experiments; E.H. and X.Y. performed the XAS analysis; S.B. and K.-W.N. performed the thermal experiments. R.L. and H.L.X. performed the STEM experiments and wrote the discussion part related to the STEM experiment. X.B. and J.L. performed the DEMS measurements. E.H. wrote the manuscript with critical input from all other authors; X.-Q.Y., X.Y., H.L.X. and J.L. edited and finalized the manuscript.

Competing interests

The authors declare no competing interests.

Additional information